AIMS Materials Science, 11(4): 605–619.
DOI: 10.3934/matersci.2024031
Received: 22 May 2024
Revised: 04 July 2024
Accepted: 11 July 2024
Published: 17 July 2024

https://www.aimspress.com/journal/Materials

Research article

Improved photovoltaic properties of $((CH_3NH_3)_{1-x}Cs_x)_3Bi_2I_9$: (x = 0–1.0) hybrid perovskite solar cells via a hot immersion method

M. F. Achoi[1], S. Kato[2], N. Kishi[2] and T. Soga[2,*]

[1] Faculty of Applied Sciences, Universiti Teknologi MARA, Cawangan Sabah, Kampus Kota Kinabalu, Sabah 88997, Malaysia
[2] Department of Electrical and Mechanical Engineering, Nagoya Institute of Technology, Nagoya, Aichi 466-8555, Japan

*** Correspondence:** Email: soga@nitech.ac.jp; Tel: +81-52-735-5532.

Abstract: To date, the lead-free perovskite has shown remarkable progress in solar cell development owing to its outstanding properties. Here, we report on the structural, optical, and photovoltaic properties of methylammonium bismuth iodide ($(CH_3NH_3)_3Bi_2I_9$, MBI) and cesium bismuth iodide ($Cs_3Bi_2I_9$, CBI) hybrid perovskite solar cells (HPeSCs) fabricated using the hot immersion method (HIM) with changing the composition x, $((CH_3NH_3)_{1-x}Cs_x)_3Bi_2I_9$; from x = 0 to x= 1.0. The compact MBI and CBI films were successfully fabricated on FTO glass substrates at x = 0 and x = 1, respectively. On the other hand, the CBI/MBI mixed structure with a rough surface was obtained in the range from x = 0.2 to x = 0.8. An incorporation of CBI in MBI showed improvement, especially in optical properties, indicating that the absorption region was extended toward a longer wavelength region with increasing x. Interestingly, the open-circuit voltage of the hybrid cell was higher than that of the MBI or CBI cell, whereas the short-circuit current was lower than that of the MBI or CBI cell. This work provides alternative ways to fabricate lead-free PeSCs using a simple and low-cost method in the future.

Keywords: perovskite solar cell; Pb-free; methylammonium bismuth iodide; cesium bismuth iodide; hybrid; hot immersion method

1. Introduction

Over the last two decades, Pb-based perovskite solar cells (PeSCs) have attracted a great deal of attention by researchers due to a promising material, producing high efficiency and performance of the solar cell device [1,2]. However, some of the weaknesses, such as toxicity [3,4] and low stability [3,5], have limited their commercialization of PeSCs until now. Furthermore, Pb-based perovskite has been shown to be sensitive to degradation due to high temperature and moisture [6,7]. Since then, in the last few years, hybrid organic-inorganic perovskite solar cells have attracted a great deal of attention among researchers in the field due to their properties such as high light absorption [8], tunable optical bandgap [6], low-cost PeSCs technology [9], and long charge carrier lifetime [10].

Bismuth-based perovskite has gained attention for the replacement of Pb recently. This is due to Bi^{3+} is non-toxic material [11] that forms a stable element [10,12], which leads to stable $6s^2$ valences electrons, and it has a similar electron configuration compared to Pb^{2+} [13]. Much effort has been made to improve the performance of MBI PeSCs, but their performance is low at present [14–16]. Since MBI PeSCs have shown poor morphology and low performance, especially output voltage, several approaches have been reported. For example, B. W. Park et al. found a granular and grain boundary surface morphology in their sample of Bi-based hybrid PeSCs [10]. S. S. Shin et al. reported on an MBI film with poor surface coverage despite applied antisolvent [17], while S. M. Jain et al. found a lack of crystallinity and a large grain size of Bi-PeSCs, which were fabricated using a vapor-assisted solution process [18]. On the other hand, Cs^+ cation-based PSCs have shown excellent optical properties [19] and excellent thermal stability [20]. However, the CBI shows a hexagonal-shaped structure and causes morphology leaving an empty space between the hexagonal-shaped structure. Consequently, it resulted in poor performance of solar cell devices. For example, Z. Ma et al. found a non-uniform surface with hexagonal shape-structure of perovskite film-based cesium [21]. Similarly, D. B. Khadka et al. reported rough surface morphology with small granular crystals of cesium bismuth iodide [22], while P. Mariyappan et al. reported the fabrication of CBI using antisolvent to improve the morphology of the perovskite film [13].

Both compounds have a similarity in terms of structure, which has a bioctahedral structure that shares the face of binuclear $(Bi_2I_9)^{3-}$and then surrounded by MA^+ or Cs^+ cations [23]. In addition, cesium cation has a smaller ionic radius compared to methylammonium as reported by I. Borriello et al. [24], while according to G. Eperon et al. introducing a cation would result in a reduction in the band gap [25]. Therefore, the hybridization process is an advantage in improving the surface morphology and optical properties. B. W. Park et al. reported that Cesium cation has improved the light absorption spectrum of the perovskite [10]. This may result in an improvement of hybrid-based solar cell device performance. It is well known that the bandgap of CBI is smaller than that of MBI [19]. Moreover, incorporation of Cesium (Cs^+) has shown a change in light absorption, as reported by G. E. Eperon et al. [25]. According to H. Choi et al., Cs mixed with MA proves that the performance of perovskite solar cell was improved [26]. It means that cesium becomes a favor for hybridization due to the radius of Cs^+ being close to MA [27].

In recent studies, there have been many reports on cesium incorporated with Pb-based hybrid perovskite solar cells (HPeSCs). For example, D. P. McMeekin et al. reported on the cesium incorporated lead bromide-iodide cell to improve the stability [28]. C. Yi et al. reported that adding Cs^+ to $FAPbI_3$ and $CsPbI_3$ increases the entropic stabilization of PeSCs [29]. While JW. Lee et al. reported on replacing HC $(NH_2)^{2+}$ with HC $(NH_2)_2PbI_3$ to improve the moisture stability of the

perovskite film [30]. In addition, Y. Cai et al. reported the fabrication of mixed cations between FA and Cs for $Pb(SCN)_2$PeSCs [31]. However, all these works used Pb-based PeSCs, which are unstable and toxic materials [32]. It may be harmful to the environment and not suitable for solar cell application in ambient air. Eventually, lead-based perovskites have limited their commercial development now. Recently, Pb-free $Cs_3Bi_2I_9$-$(MA)_3Bi_2I_9$ hybrid perovskite solar cell was reported with improved performance using spin coating. However, the detailed mechanism of improvement has not been clarified yet [33].

For the fabrication of PeSCs, it is very important to determine the quality of film produced for PeSCs development. The quality of the film is a key to the better performance of the solar cell device, and it depends on the type of fabrication method being employed. Perovskite film is often prepared by spin coating with antisolvent to obtain high-crystalline films. We have shown that pinhole-free MBI films can be synthesized by a simple hot immersion method (HIM) in 2021 [34] and have presented the preliminary results of MBI solar cells recently [35]. It is a simple method without using an antisolvent to fabricate a compact and pinhole-free Pb-free perovskite absorber layer for solar cell application. Very recently, we reported $(CH_3NH_3)_{1-x}Cs_x)_3Bi_2I_9$ hybrid perovskite solar cells with changing x from 0 to 1.0 by spin coating. The improvement in photovoltaic properties was observed with hybrid structure, but the chlorobenzene treatment condition to prepare the pinhole-free film is severe. Furthermore, the power conversion efficiency obtained was low [36]. Compared with spin coating, the advantage of HIM is the simplicity in preparing pinhole-free films [34]. Moreover, the consumption of precursors is less, which suggests the possibility of producing perovskite solar cell at low cost. In the present work, we have fabricated the lead-free $((CH_3NH_3)_{1-x}Cs_x)_3Bi_2I_9$ hybrid perovskite solar cell with a change of the ratio from x = 0 to x = 1.0 by HIM for the first time. We incorporate CBI into MBI without using an antisolvent, and then we investigate the effect of the CBI ratio in the MBI/CBI hybrid film. As a result, we managed to improve the device performance of lead-free PeSCs; especially the open circuit voltage was greatly improved by the hybrid cell. The structural, optical and photovoltaic properties of $((CH_3NH_3)_{1-x}Cs_x)_3Bi_2I_9$ perovskite films are reported with x change in the range from 0 to 1.

2. Materials and methods

The preparation of FTO glass substrate and the fabrication of P3HT as a hole transport layer (HTL) and TiO_2 as an electron transport layer (ETL) are referred to Ref. 37. Precursors of both compounds, CBI and MBI, were prepared, where the preparation of the MBI solution is referred to our previous reported work [37], while for the CBI, CsI and BiI_3 precursors (both purchased from Sigma-Aldrich, 99.999%) were mixed in ratio [1.5:1.0] in 10 mL of DMF to form a 0.5 M CBI solution. The mixture was then continuously stirred for 1 h at 60 ℃ to allow the solution to be mixed vigorously and left for aging time. All this step is repeated for the preparation of different volume of CBI solution, with 2, 5, 8, and 10 mL. The CBI and MBI solution was then mixed to form 10 mL of hybrid solution changing the ratio x = [CBI]/([MBI] + [CBI]) = 0, 0.2, 0.5, 0.8, and 1.0. Then, the hybrid solution is stirred under continuous stirring at 800 rpm and again left for the ageing time. Furthermore, the thin films were prepared on TiO_2 coated FTO glass using HIM according to previous work reported [34]. In brief, TiO_2 coated FTO glass substrate was immersed in the hybrid solution under 70 ℃ at an immersion time of 24 h, then followed by the annealing at 100 ℃ for 10 min. Last, the fabrication of P3HT as an HTL and carbon electrode is mentioned [37] and is followed by the silver paste on the

carbon layer. The whole fabrication process was carried out in a dry nitrogen-filled glovebox except for the silver paste and colloidal graphite deposition.

The structure and morphology of HPeSCs were characterized by X-ray diffractometer (XRD) (Rigaku RINT-2100 diffractometer) and scanning electron microscopy (SEM) (JEOL JSM-7600F), respectively, while the optical properties and the performance of the solar cells were characterized by UV-vis spectrophotometer (JASCO Model V-570) and the solar simulator under simulated solar light illumination (AM 1.5, 100 $mW \cdot cm^{-2}$), respectively. Finally, the thickness of the film was measured using the Dektak measurement (Veeco-Dektak 150).

3. Results

Figure 1 shows the XRD curves of HPeSCs at different CBI composition, x. The peaks corresponding to the hexagonal structure of the CBI and MBI (P63/mmc) are observed. They have a zero-dimensional structure with isolated bioctahedrons [38]. All the XRD peaks are indexed as a hexagonal MBI (ICDD PDF Card no. 01–084-8254) [39,40] and CBI (ICDD PDF Card no. 04-008-8708) [21]. The XRD main peak information of the ICDD cards for MBI and CBI is summarized in Table 1. At x = 0, all XRD curves exhibit MBI peaks, which are 11.89, 12.67, 14.40, 16.40, 24.58, 32.29, 43.37 and 44.71^o assigned to (110), (111), (112), (113), (006), (206), (400) and (049) lattice planes [34], respectively. As for incorporated CBI in MBI at x = 0.2, the crystalline phase is changed and combined as a one crystalline phase. As can be seen in Figure 1b, 12.82, 25.86, 27.54, 29.68, 32.40, 42.12, 42.92 and 45.79^o, were corresponding to (101), (202), (203), (204), (205), (208), (220) and (209) lattice planes for CBI [22], respectively. This occurred because of no phase segregation since both compound compositions fit to the P63/mmc space group with a hexagonal crystal system [33]. As for increased the composition of CBI in MBI at x = 0.5, the CBI peaks at 25.86, 29.68, 32.44, and 42.92^o are slowly increased [33], as can be observed in Figure 1c. These peaks increase in intensity further with a narrower peak at x = 0.8, and a new peak is detected at 21.22^o, belonging to the CBI peak, as shown in Figure 1d. Finally, at x = 1.0, the peaks at 12.82, 21.22, 25.86, 27.54, 29.68, 32.40, 42.12, 42.92, and 45.79^o appeared as dominant, sharp and a narrow peak [33]. However, there is no significant variation in the peak position for different CBI compositions, which is consistent with the results by spin coating [33]. From this result, we can observe that the crystallinity of CBI increases gradually with increasing CBI composition of the solution. The oxidized bismuth compound exists in MBI at x = 0, which is BiOI and Bi_2O_3 at 29.60 (012) and 31.70^o (110) [41], respectively, as shown in Figure 1a. This means that MBI is easily oxidized in the ambient air. However, after the incorporation of CBI into MBI, the stability of perovskite solar cell is improved, where no peak of oxidized bismuth is seen in Figure 1b–e. This means that the high stability of HPeSCs in ambient air is expected with hybrid cells.

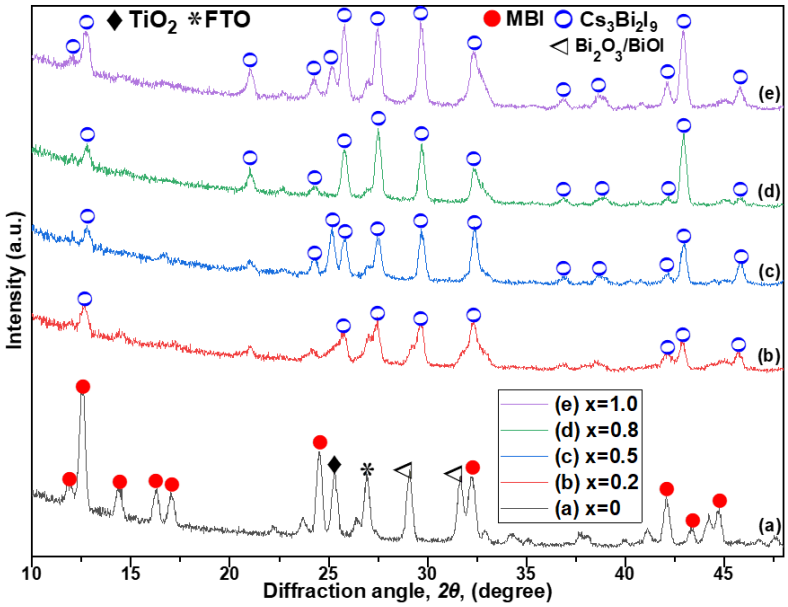

Figure 1. XRD curves of HPeSCs for different CBI compositions x.

Table 1. ICDD card data for MBI and CBI.

	2θ (deg)	Intensity	h	k	l
MBI	11.909	162	1	1	0
	12.584	1000	1	1	1
	14.437	329	1	1	2
	16.292	43	0	0	4
	17.076	284	1	1	3
	24.542	179	0	0	6
	25.333	385	2	2	2
	32.307	354	2	0	6
	42.101	335	4	0	0
	44.704	209	0	4	9
CBI	12.151	165	1	0	0
	12.851	574	1	0	1
	21.126	245	1	1	0
	24.289	279	1	0	5
	25.204	451	0	0	6
	25.867	910	2	0	2
	27.552	1000	2	0	3
	29.764	949	2	0	4
	32.406	685	2	0	5
	37.024	54	3	0	0
	38.665	159	2	0	7
	42.171	279	2	0	8
	43.015	746	2	2	0
	45.878	394	2	0	9

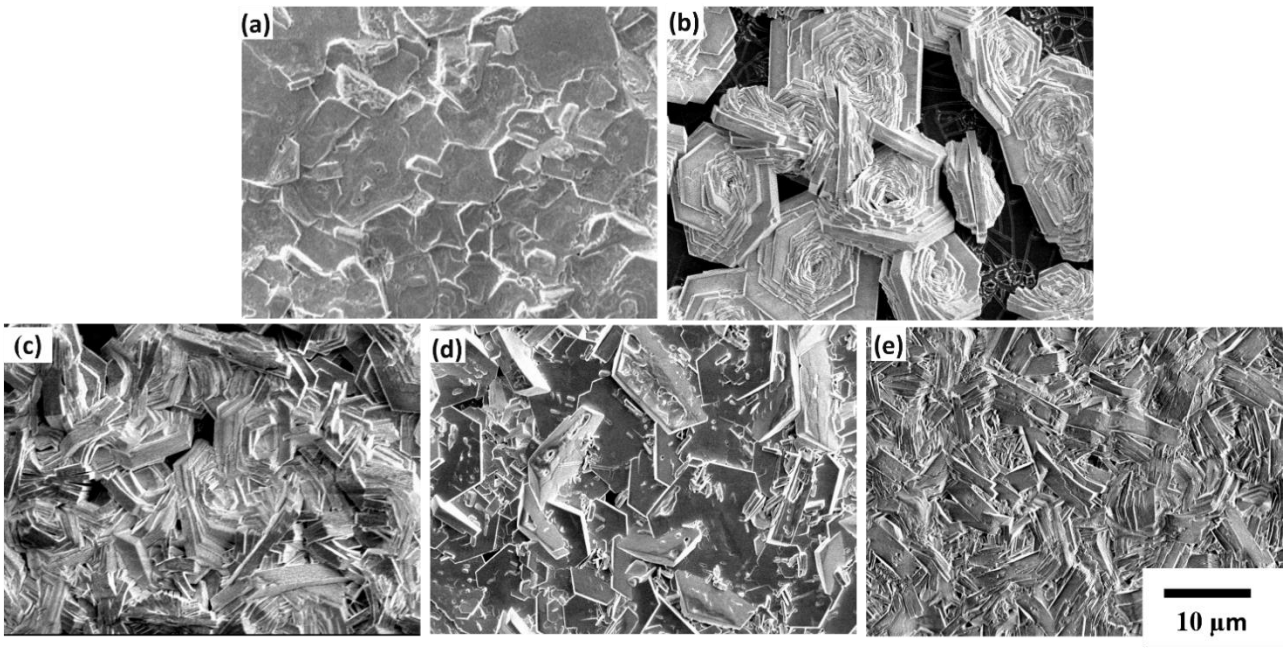

Figure 2. SEM images of HPeSCs for different CBI compositions, x: (a) x = 0, (b) x = 0.2, (c) x = 0.5, (d) x = 0.8 and (e) x = 1.0.

Figure 2 visually depicts the SEM images of HPeSCs at different CBI compositions. At x = 0, as confirmed by the XRD result, the MBI film is compact and pinhole-free, as shown in Figure 2a. However, at x = 0.2 of CBI, it can be seen that the morphological phase is absolutely changed. This means that the CBI starts to take over the MBI phase as confirmed by the XRD result in Figure 1b. Corresponding to that, the hexagonal shape of the CBI starts to be seen. The hexagonal shape is assigned to CBI [21], and not many hexagonal shapes are seen at low amounts of CBI (x = 0.2) instead leaving an empty space between the hexagonal shapes, as shown in Figure 2b. However, the amount of hexagonal CBI starts to increase as the CBI ratio increases to x = 0.5. As confirmed by XRD (Figure 1c) the peak slowly increases in intensity at 25.86, 29.68, 32.44, and 42.92º. This hexagonal shape is seen to be sinking to each other, destructive and combined continuously, then start to form a film. The amount of CBI and MBI causes the empty space equally as previously seen, which is slowly reduced, as shown in Figure 2c. This is due to the density of hexagonal CBI starting to grow larger and closer to each other, and it is caused by the nucleation growth and crystallization process [39]. As for an additional increase in the amount of CBI at x = 0.8, the CBI grew largely as encouraged by the nucleation growth. In addition, CBI growth is assisted by the continuous temperature below 70 ℃ during the hot immersion process. This time, the hexagonal shapes are close to each other and overlapped, causing the destructive hexagonal shapes of the CBI and it forms an island-like structure, as can be seen in Figure 2d. Consequently, the surface is not smooth, which presents holes, and some of the hexagonal shape edges are out of the surface as compared to Figure 1a. This indicates that the CBI hexagonal shape is not fully yet combined and sank to each other, but no empty space is left as seen earlier. Finally, at x = 1.0 of the CBI composition, interestingly the formation of compact and pinhole-free film is clearly seen. Furthermore, it is continuous growth of CBI with a dense surface, compared to the composition of the CBI at x = 0.2 and x = 0.5. The Dektak measurement showed that the thickness of the MBI film (x = 0) and the CBI film (x = 1) is 621 and 818 nm, respectively. This

time, no peeling of the surface can be seen, and no hexagonal shape can be seen, which is formed due to the interdiffusion process [42]. Moreover, it happened because Cs is an enlarged crystal grain and consequently improves perovskite crystallization, as reported by C. Yi et al. [29]. Our XRD result agrees well with this finding, where the crystallinity of HPeSCs shows improvement, as can be observed in Figure 1e. In summary, the formation of a compact film without holes can be obtained by HIM without the hybrid cell, at x = 0 and 1.0. Instead, with hybrid cells, an island-like structure is obtained at $0.2 \leq x \leq 0.8$.

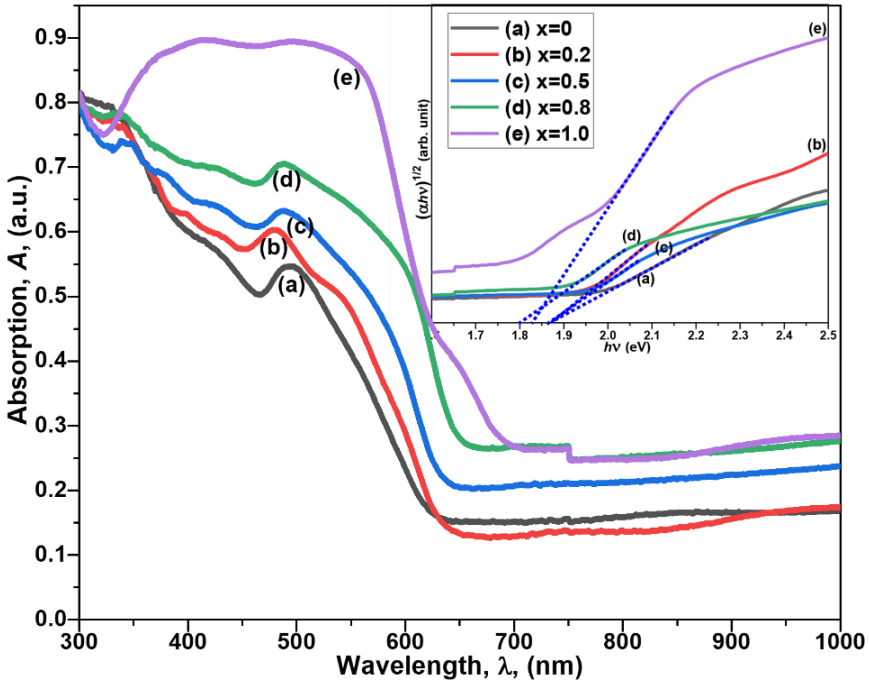

Figure 3. Absorption spectra of HPeSCs for different CBI compositions, x. Inset is Tauc plot.

Figure 3 shows the optical absorption spectra of cesium incorporated hybrid bismuth-based perovskite solar cells at different CBI ratios, while the inset shows the optical bandgap as determined by a Tauc plot [28]. The trend of an increase in absorbance intensity is observed as the CBI ratios change from x = 0 to x = 1.0. This clearly indicates that the CBI ratio influences the absorbance in the visible wavelength region of fabricated lead-free PeSCs. This happened because Cs^+ has hung the light absorption spectrum of PeSCs, and this may improve the device performance [10]. On the other hand, Figure 3 shows that the MBI absorbance wavelength region is around 600 nm, which is similar to previous work [37]. However, after the incorporation of CBI into MBI, the absorption range is slightly shifted to longer wavelength side, from 600 to around 650 nm due to the amount of added-CBI into the MBI perovskite, as can be seen in Figure 3b–d. According to F. Ünlü et al. the Cs influences the MBA bandgap, changes the absorption ranges, and pristine CBI shows the highest absorption because Cs^+ leads to a reduction in the band gap [33]. Our result agrees well with this finding, which shows that high absorption is recorded for the CBI ratio at x = 1.0. Consequently, a better compact and pinhole-free morphology has been attributed to the better and high absorption, as visually depicted in the SEM images of Figure 2e. Interestingly, it can be observed that the absorption region extended into the infrared region with an optical bandgap of 1.83 eV at x = 1.0, as shown in the inset of Figure 3e.

This means that the harvesting of light is improved in the CBI based PeSCs device [17], which produces more light from the device. Also, our bandgap value obtained at x = 1.0, is a little lower than those previously reported, for example F. Ünlü et al. reported that the bandgap for $Cs_3Bi_2I_9$ is 2.30 eV, which was fabricated using solution spin coating [33], while B. W. Park et al. found 2.2 eV with fabricated PeSCs via spin-coating method [10] and D. B. Khadka et al. found 2.08 eV in their sample, which was fabricated using the solution process [22]. The bandgap of HPeSCs via HIM is slightly smaller than that via the spin coating. This will be due to the variation in composition and/or crystal orientation as observed by XRD [36]. This difference was ~~be~~ due to the hot immersion method used in this work. This clearly elucidates that to fabricate lead-free PeSCs, the best optical properties can be achievable using HIM with a narrow band gap and high absorption of light, which may influence the solar cell performance. In summary, the optical properties of HPeSCs change, with changing the CBI ratios from x = 0 to x = 1.0.

Figure 4 indicates the J-V characteristics of HPeSCs at different CBI ratios, while the inset is the solar cell structure. It can be seen from the J-V curves that the current density and the voltage value change as CBI is included in MBI, from x = 0 to x = 1.0. The short circuit current density (J_{sc}), the open circuit voltage (V_{oc}), the fill factor (FF), and the power conversion efficiency (PCE) are plotted in Figure 5 for different CBI ratios. At x = 0, the open circuit voltage is 0.17 V and shows a further upward trend up to 0.67 V at x = 0.8 of the CBI ratio, and then the V_{oc} dropped to 0.26 V, at x = 1.0, as shown in Figure 5b.

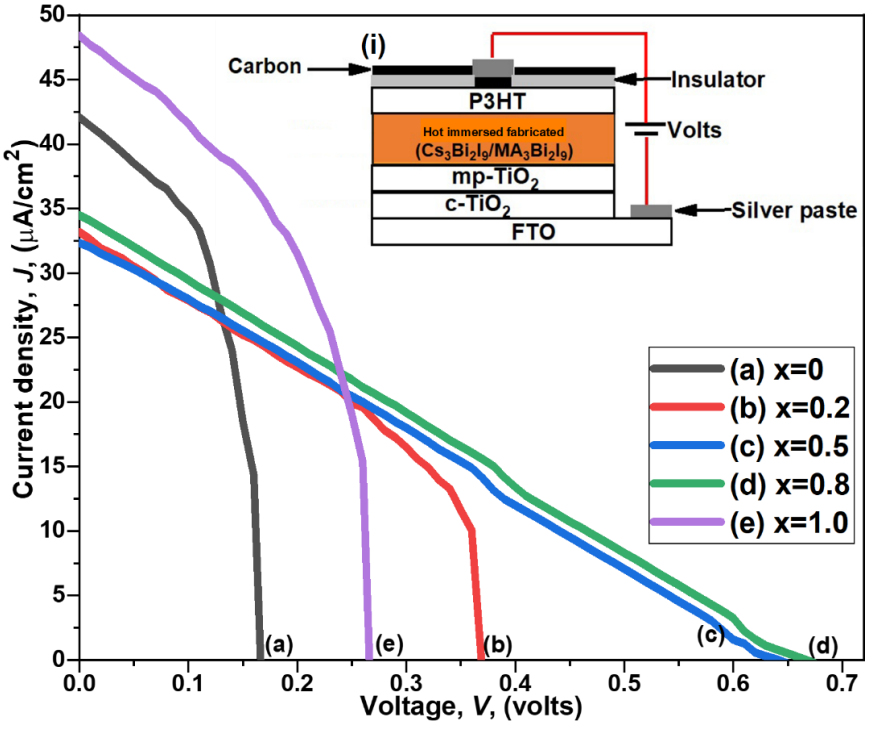

Figure4. J-V curves of HPeSCs for different CBI compositions, x. Inset is the schematic diagram of the HPeSC.

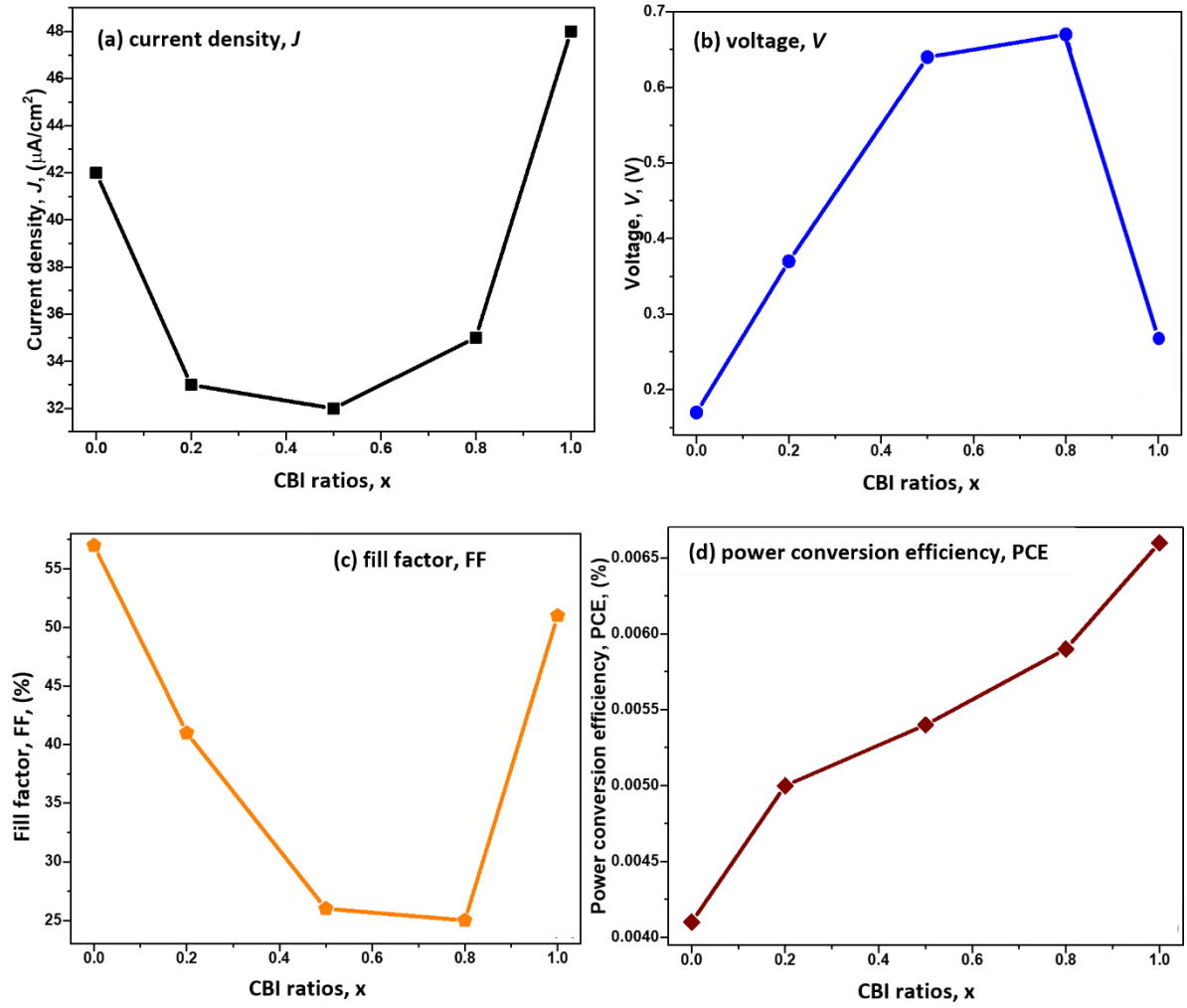

Figure 5. Solar cell parameters for HPeSCs at different CBI compositions, x.

However, an opposite trend is observed in short circuit current, J_{sc}, and fill factor FF, which show an increase trend at x = 0 and 1.0 as compared to V_{oc}, as can be seen in Figure 5a and c. In the case of the CBI ratio at x = 0 and 1.0, it recorded the FF and J_{sc} values much better than other CBI ratios ($0.2 \leq x \leq 0.8$), especially the J_{sc} and FF values are 48 μA/cm^2 and 51% at x = 0, respectively. Eventually, it clearly shows the gradual improvement in power conversion efficiency (PCE) from 0.004% to 0.006% with increasing CBI ratio from 0 to x = 1, as shown in Figure 5d.

4. Discussion

The surface morphology, optical properties, and solar cell performance of HPeSCs at different compositions were described in the previous chapter. The results are summarized as follows.

(1) The surface is compact and smooth at x = 0 and 1, while the surface morphology is rough, and the film is composed of both large hexagonal crystals and small crystals.

(2) The optical bandgap decreases slightly from 1.9 to 1.8 eV with increasing x from 0 to 1.

(3) The short circuit current density and FF are large at x = 0 and 1, whereas they are small at x = 0.2, 0.5 and 0.8. It shows "U" shape.

(4) The open circuit voltage is high at x = 0.2, 0.5 and 0.8, while it is low at x = 0 and 1. It shows "∩" shape.

Before discussing the photovoltaic properties, the surface morphologies for different CBI ratios are analyzed. As shown in Figure 2, the surface morphology is smooth without pinholes at x = 0. This means that the film is composed of small crystals homogeneously. At x = 0.2, large hexagonal crystals appear other than the smooth film. The hexagonal crystals will be CBI, which is usually seen in a spin-coated CBI film [21]. The density of the CBI crystal increases with increasing x, and again the surface becomes flat at x = 1. The change in surface morphology is schematically illustrated in Figure 6.

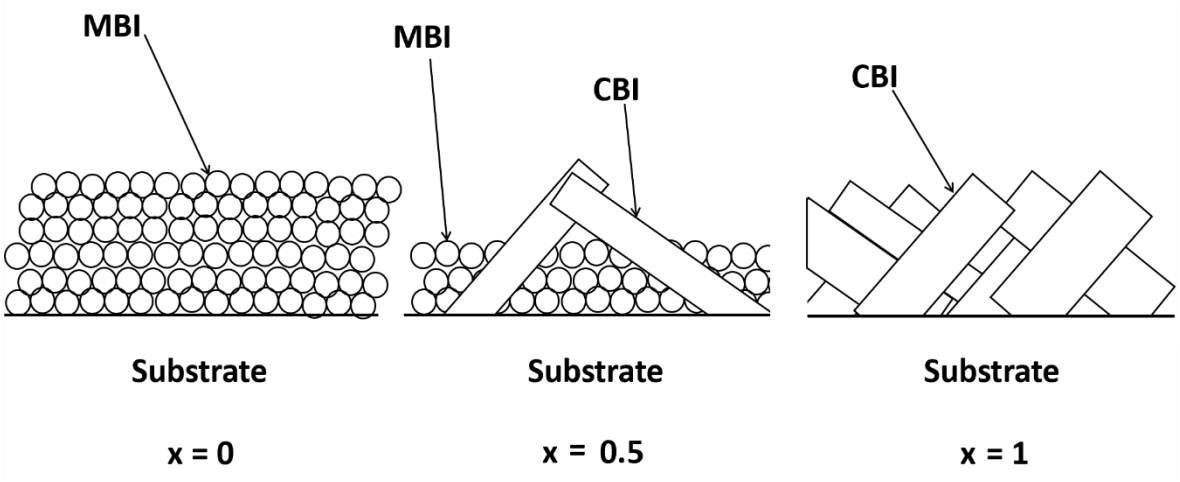

Figure 6. Schematic illustration of HPeSC morphologies for different CBI compositions x.

Next, the photovoltaic properties of hybrid solar cells for different CBI ratio are discussed. Let us first check the behavior of FF. FF decreases with an increase in the ratio from x = 0 to 0.8 rapidly. The possible reasons for the decrease in FF are the increase in series resistance or the decrease in parallel resistance in the equivalent circuit [43]. The increase in series resistance occurs via the additional resistance component, and the decrease in parallel resistance occurs via the increase in the pinhole or defect density of the perovskite film. If the second reason is correct, the open circuit voltage should decrease with increasing the CBI ratio because the saturation current J_0 increases from the Eq 1 [43].

$$V_{oc} = kT/q \ln(J_{sc}/J_0 + 1) \quad (1)$$

However, the open circuit voltage increases at x = 0.2, 0.5 and 0.8. This means that the decrease of FF is not due to the decrease in parallel resistance but to the increase in series resistance. The decrease of short circuit current at 0.2, 0.5, and 0.8 should be also explained by the increase of series resistance. The FF and the short circuit current again increase at x = 0, probably due to the recovery of series resistance.

The increase in open circuit voltage from x = 0 to 0.8 is due to the decrease in saturation current J_0, as shown in Eq 1. This would be due to the low leakage current of the MBI/CBI hybrid films. The mechanism of low leakage current is not clarified, but Cs-doped MBI and methylammonium-doped CBI would contribute to the low defect density, resulting in improvement. Since the power conversion efficiency is proportional to the product of J_{sc}, V_{oc}, and FF, the power conversion efficiency gradually increases with CBI ratio from x = 0 to 1 as shown in Figure 5d. Our results show that the series

resistance increases by Cs-doping in MBI and methylammonium-doping in CBI. The open circuit voltage was improved, while the short circuit current and the fill factor became worse with MBI-CBI hybrid cell in this work. To get high J_{sc}, V_{oc} and *FF* simultaneously for high power conversion efficiency, the improvement of J_{sc} and *FF* is very important. For this purpose, the development of element doping to get low resistivity film is necessary. Then J_{sc}, V_{oc} and *FF* will increase with hybrid structure, resulting in the improvement of power conversion efficiency in the future.

Finally, the PCE of $(CH_3NH_3)_{1-x}Cs_x)_3Bi_2I_9$ HPeSCs by HIM are briefly compared with the literature. F. Ünlü et al reported a drastic improvement of PCE from 0.22% of $(CH_3NH_3)_3Bi_2I_9$ to 1.50% of $(CH_3NH_3)_{0.9}Cs_{0.1})_3Bi_2I_9$ [33]. It corresponds to about 7 times improvement. On the other hand, our result showed only 1.2–1.3 times improvement from $(CH_3NH_3)_3Bi_2I_9$ to $(CH_3NH_3)_{0.8}Cs_{0.2})_3Bi_2I_9$. However, it is interesting to note that the open circuit voltage is slightly higher, and the short circuit current is slightly lower than those fabricated by spin coating with chlorobenzene treatment. This was due to the difference in the properties of the materials, such as crystal orientation, defect density, resistivity, etc. [36]. The highest CBI based solar cell as ever reported is $Cs_3Bi_2I_9$-$Ag_3Bi_2I_9$ hybrid cell with PCE of 3.59% [44], which is higher than that of the state-of-the-art CBI or MBI cell (3.2%) [45]. On the other hand, the PCE of HPeSCs via HIM is much lower than that fabricated by spin coating. The possible reasons will be deposition of amorphous component which isn't detected by XRD, high resistivity film, etc. The electrode made of Ag paste may also degrade the device performance, while electrode is usually formed by vacuum evaporation. The effects of hybridization on the photovoltaic properties of bismuth-based perovskite solar cell have not been studied very much in comparison to those of Pb-based perovskite solar cell. However, there is a possibility to increase PCE of Bi-based PeSCs. The stability of HPeSCs have not been studied either. The improvement not only in PCE but also in stability is expected in the future by getting knowledge on hybridization of perovskite material through the fundamental study of hybrid perovskite solar cells.

5. Conclusions

We have successfully fabricated and evaluated the HPeSCs by changing the CBI ratio x using a low-cost and simple HIM, for the first time. We found that the fabrication of a compact film and pinhole-free can be obtained at x = 0 and 1.0, while the surface morphology was rough at x = 0.2, 0.5 and 0.8. The extended absorption region shifted towards a longer wavelength with increasing x. The short circuit current of CBI and MBI cells is higher than that of the hybrid cell, but the open circuit voltage of the hybrid cell is higher than those of the CBI and MBI cell. The improvement in open circuit voltage at x = 0.2, 0.5 and 0.8 was predicted to be due to the hybrid effect of MBI and CBI. As a result, the performance of lead-free PeSCs is achievable with the best efficiency at x = 1.0. The hybridization of two materials will be a useful approach to improve the properties of Pb-free perovskite solar cells in the future.

Use of AI tools declaration

The authors declare they have not used Artificial Intelligence (AI) tools in the creation of this article.

Acknowledgments

The authors are grateful for the financial support from Japanese government (MEXT Scholarship) and the Universiti Teknologi MARA (UiTM).

Conflict of interest

T. Soga is editorial board member for *AIMS Materials Science* and was not involved in the editorial review or the decision to publish this article. The authors declare no conflict of interest.

References

1. Burschka J, Pellet JN, Moon SJ, et al. (2013) Sequential deposition as a route to high-performance perovskite-sensitized solar cells. *Nature* 499: 316–319. https://doi.org/10.1038/nature12340
2. Yang WS, Park BW, Jung EH, et al. (2017) Iodide management in formamidinium-lead-halide–based perovskite layers for efficient solar cells. *Science* 356: 1376–1379. https://doi.org/10.1126/science.aan2301
3. Wang Z, Lin Q, Chmiel FP, et al. (2017) Efficient ambient-air-stable solar cells with 2D–3D heterostructured butylammonium-caesium-formamidinium lead halide perovskites. *Nat Energy* 2: 17135. https://doi.org/10.1038/nenergy.2017.135
4. Rong Y, Hu Y, Mei A, et al. (2018) Challenges for commercializing perovskite solar cells. *Science* 361: 6408. https://doi.org/10.1126/science.aat8235
5. Cheacharoen R, Rolston N, Harwood D, et al. (2018) Design and understanding of encapsulated perovskite solar cells to withstand temperature cycling. *Energy Environ Sci* 11: 144–150. https://doi.org/10.1039/C7EE02564E
6. Noh JH, Im SH, Heo JH, et al. (2013) Chemical management for colorful, efficient, and stable inorganic–organic hybrid nanostructured solar cells. *Nano Lett* 13: 1764–1769. https://doi.org/10.1021/nl400349b
7. Stoumpos CC, Malliakas CD, Kanatzidis MG (2013) Semiconducting tin and lead iodide perovskites with organic cations: Phase transitions, high mobilities, and near-infrared photoluminescent properties. *Inorg Chem* 52: 9019–9038. https://doi.org/10.1021/ic401215x
8. Kojima A, Teshima K, Shirai Y, et al. (2009) Organometal halide perovskites as visible-light sensitizers for photovoltaic cells. *J Am Chem Soc* 131: 6050–6051. https://doi.org/10.1021/ja809598r
9. Snaith HJ (2013) Perovskites: The emergence of a new era for low-cost, high-efficiency solar cells. *J Phys Chem Lett* 4: 3623–3630. https://doi.org/10.1021/jz4020162
10. Park BW, Philippe B, Zhang X, et al. (2015) Bismuth based hybrid perovskites $A_3Bi_2I_9$ (A: Methylammonium or cesium) for solar cell application. *Adv Mater* 9: 6806–6813. https://doi.org/10.1002/adma.201501978
11. Sano Y, Satoh H, Chiba M, et al. (2005) Oral toxicity of bismuth in rat: Single and 28-day repeated administration studies. *J Occup Health* 47: 293–298. https://doi.org/10.1539/joh.47.293
12. Lyu M, Yun J, Cai M, et al. (2016) Organic–inorganic bismuth (III)-based material: A lead-free, air-stable and solution-processable light-absorber beyond organolead perovskites. *Nano Res* 9: 692–702. https://doi.org/10.1007/s12274-015-0948-y

13. Mariyappan P, Chowdhury TH, Subashchandran S, et al. (2020) Fabrication of lead-free $CsBi_3I_{10}$ based compact perovskite thin films by employing solvent engineering and anti-solvent treatment techniques: An efficient photo-conversion efficiency up to 740 nm. *Sustain Energ Fuels* 4: 5042–5049. https://doi.org/10.1039/D0SE00786B
14. Slavney AH, Hu T, Lindenberg AM, et al. (2016) A bismuth-halide double perovskite with long carrier recombination lifetime for photovoltaic applications. *J Am Chem Soc* 138: 2138–2141. https://doi.org/10.1021/jacs.5b13294
15. Khazaee M, Sardashti K, Chung CC, et al. (2019) Dual-source evaporation of silver bismuth iodide films for planar junction solar cells. *J Mater Chem A* 7: 2095–2105. https://doi.org/10.1039/C8TA08679F
16. Sanders S, Stümmler D, Pfeiffer P, et al. (2019) Chemical vapor deposition of organic-inorganic bismuth-based perovskite films for solar cell application. *Sci Rep* 9: 9774. https://doi.org/10.1038/s41598-019-46199-4
17. Shin S, Baena JPC, Kurchin RC, et al. (2018) Solvent-engineering method to deposit compact bismuth-based thin films: Mechanism and application to photovoltaics. *Chem Mater* 30: 336–343. https://doi.org/10.1021/acs.chemmater.7b03227
18. Jain SM, Phuyal D, Davies ML, et al. (2018) An effective approach of vapour assisted morphological tailoring for reducing metal defect sites in lead-free, $(CH_3NH_3)_3Bi_2I_9$ bismuth-based perovskite solar cells for improved performance and long-term stability. *Nano Energy* 49: 614–624. https://doi.org/10.1016/j.nanoen.2018.05.003
19. Johansson MB, Zhu H, Johansson EMJ (2016) Extended photo-conversion spectrum in low-toxic bismuth halide perovskite solar cells. *J Phys Chem Lett* 7: 3467–3471. https://doi.org/10.1021/acs.jpclett.6b0145
20. Kulbak M, Cahen D, Hodes G (2015) How important is the organic part of lead halide perovskite photovoltaic cells? Efficient $CsPbBr_3$ cells. *J Phys Chem Lett* 6: 2452–2456. https://doi.org/10.1021/acs.jpclett.5b00968
21. Ma Z, Peng S, Wu Y, et al. (2017) Air-stable layered bismuth-based perovskite-like materials: Structures and semiconductor properties. *Physica B* 526: 136–142. https://doi.org/10.1016/j.physb.2017.08.079
22. Khadka DB, Shirai Y, Yanagida, et al. (2019) Exploring the effects of interfacial carrier transport layers on device performance and optoelectronic properties of planar perovskite solar cells. *J Mater Chem* C 7: 8335–8343. https://doi.org/10.1039/C7TC02822A
23. Öz S, Hebig JC, Jung E, et al. (2016) Zero-dimensional $(CH_3NH_3)_3Bi_2I_9$ perovskite for optoelectronic applications. *Sol Energy Mater Sol Cells* 158: 195–201. https://doi.org/10.1016/j.solmat.2016.01.035
24. Borriello I, Cantele G, Ninno D (2008) Ab initio investigation of hybrid organic-inorganic perovskites based on tin halides. *Phys Rev B* 77: 235214. https://doi.org/10.1103/PhysRevB.77.235214
25. Eperon GE, Stranks SD, Menelaou C, et al. (2014) Formamidinium lead trihalide: A broadly tunable perovskite for efficient planar heterojunction solar cells. *Energy Environ Sci* 7: 982–988. https://doi.org/10.1039/C3EE43822H
26. Choi H, Jeong J, Kim HB, et al (2014) Cesium-doped methylammonium lead iodide perovskite light absorber for hybrid solar cells. *Nano Energy* 7: 80–85. https://doi.org/10.1016/j.nanoen.2014.04.017

27. Si J, Liu Y, Wang N, et al. (2017) Green light-emitting diodes based on hybrid perovskite films with mixed cesium and methylammonium cations. *Nano Res* 10: 1329–1335. https://doi.org/10.1007/s12274-017-1432-7
28. McMeekin DP, Sadoughi G, Rehman W, et al. (2016) A mixed-cation lead mixed-halide perovskite absorber for tandem solar cells. *Science* 351: 151–155. https://doi/10.1126/science.aad5845
29. Yi C, Luo J, Meloni S, et al. (2016) Entropic stabilization of mixed A-cation ABX_3 metal halide perovskites for high performance perovskite solar cells. *Energy Environ Sci* 9: 656–662. https://doi.org/10.1039/C5EE03255E
30. Lee JW, Kim DH, Kim HS, et al. (2015) Formamidinium and cesium hybridization for photo- and moisture-stable perovskite solar cell. *Adv Energy Mater* 5: 1501310. https://doi.org/10.1002/aenm.201501310
31. Cai Y, Wang S, Sun M, et al (2018) Mixed cations and mixed halide perovskite solar cell with lead thiocyanate additive for high efficiency and long-term moisture stability. *Org Electron* 53: 249–255. https://doi.org/10.1016/j.orgel.2017.11.045
32. Zhang Y, Zhang Z, Yu W, et al (2022) Lead-free double perovskite $Cs_2AgIn_{0.9}Bi_{0.1}Cl_6$ quantum dots for white light-emitting diodes. *Adv Sci* 9: 2102895. https://doi.org/10.1002/advs.202102895
33. Ünlü F, Kulkarni A, Lê K, et al. (2021) Single- or double A-site cations in $A_3Bi_2I_9$ bismuth perovskites: What is the suitable choice? *J Mater Res* 36: 1794–1804. https://doi.org/10.1557/s43578-021-00155-z
34. Achoi MF, Aiba S, Kato S, et al. (2021) A novel approach towards compact and improved-crystallinity methylammonium bismuth iodide film via hot immersion method. *Mater Lett X* 12: 100096. https://doi.org/10.1016/j.mlblux.2021.100096
35. Achoi MF, Aiba S, Kato S, et al. (2022) Fabrication and properties of compact $(CH_3NH_3)_3Bi_2I_9$ perovskite solar cell by the hot immersion method. *Opt Mater X* 15: 100158. https://doi.org/10.1016/j.omx.2022.100158
36. Achoi MF, Kato S, Kishi N, et al. (2024) Properties of $((CH_3NH_3)_{1-x}Cs_x)_3Bi_2I_9$: (x = 0–1.0) hybrid perovskite solar cells with chlorobenzene treatment. *J Sol Energy Res Updates* 11: 37–44. https://doi.org/10.31875/2410-2199.2024.11.05
37. Achoi MF, Aiba S, Kato S, et al. (2021) Effect of spinning rate on the performance of multilayer bi-perovskite solar cells. *Int J Nanoelectron Mater* 14: 1–10. Available from: https://ijneam.unimap.edu.my/images/PDF/InCAPE2021/Vol_14_SI_Dec_2021_1-10.pdf.
38. Singh T, Kulkarni A, Ikegami M, et al. (2016) Effect of electron transporting layer on bismuth-based lead-free perovskite $(CH_3NH_3)_3Bi_2I_9$ for photovoltaic applications. *ACS Appl Mater Interfaces* 8: 14542–14547. https://doi.org/10.1021/acsami.6b02843
39. Ataei M, Adelifard M, Hosseini SS (2021) Physical properties and photovoltaic performance of perovskite solar cells based on lead-free $A_3Bi_2I_9$ (A = CH_3NH_3, Cs) active layers. *J Electron Mater* 50: 571–579. https://doi.org/10.1007/s11664-020-08580-2
40. Shirahata Y (2020) Effects of annealing temperature on photovoltaic properties of lead-free $(CH_3NH_3)_3Bi_2I_9$ solar cells. *J Ceram Soc Jpn* 128: 298–303. https://doi.org/10.2109/jcersj2.19156
41. Hoye RLZ, Brandt RE, Osherov A, et al. (2016) Methylammonium bismuth iodide as a lead-free, stable hybrid organic–inorganic solar absorber. *Chem Eur J* 80401: 2605–2610. https://doi.org/10.1002/chem.201505055

42. Xiao Z, Bi C, Shao Y, et al. (2014) Efficient, high yield perovskite photovoltaic devices grown by interdiffusion of solution-processed precursor stacking layers. *Energy Environ Sci* 7: 2619–2623. https://doi.org/10.1039/C4EE01138D
43. Green MA (1986) *Solar Cells: Operating Principles, Technology and System Applications*, Sydney: UNSW Press, 85–102.
44. Hu W, He X, Fang Z, et al. (2020) Bulk heterojunction gifts bismuth-based lead-free perovskite solar cells with record efficiency. *Nano Energy* 68: 104362. https://doi.org/10.1016/j.nanoen.2019.104362
45. Bai F, Hu Y, Hu Y, et al. (2018) Lead-free, air-stable ultrathin $Cs_3Bi_2I_9$ perovskite nanosheets for solar cells. *Sol Energy Mater Sol Cells* 184: 15–21. https://doi.org/10.1016/j.solmat.2018.04.032